https://doi.org/10.1016/j.tws.2021.108103

Dynamic buckling of rotationally restrained FG porous arches reinforced with graphene nanoplatelets under a uniform step load

Zhicheng Yang[1], Di Wu [2], Jie Yang[3,*], Siu-Kai Lai[4,5], Jiangen Lv[1], Airong Liu[6], Jiyang Fu[6,**]

[1] College of Urban and Rural Construction, Zhongkai University of Agriculture and Engineering, Guangzhou, 510225, China

[2] Centre for Built Infrastructure Research (CBIR), School of Civil and Environmental Engineering, University of Technology Sydney, Sydney, NSW, Australia

[3] School of Engineering, RMIT University, PO Box 71, Bundoora, VIC 3083, Australia

[4] Department of Civil and Environmental Engineering, The Hong Kong Polytechnic University, Kowloon, Hong Kong, China

[5] Hong Kong Branch of National Rail Transit Electrification and Automation Engineering Technology Research Center, The Hong Kong Polytechnic University, Kowloon, Hong Kong, China

[6] Wind and Vibration Engineering Research Center, Guangzhou University, Guangzhou, 510006, China

* Corresponding author: jie.yang@rmit.edu.au (J. Yang)

** Corresponding author: jyfu@gzhu.edu.cn (J. Fu)

Abstract: This paper presents a dynamic buckling analysis for a rotationally restrained functionally graded (FG) graphene nanoplatelets (GPLs) reinforced composite (FG-GPLRC) porous arch under a uniform step load where GPL nanofillers are uniformly dispersed while the porosity coefficient varies along the thickness direction of the arch. The effective material properties of the FG-GPLRC porous arch are determined by the volume fraction distribution of materials. Analytical solutions for the symmetric limit point dynamic buckling and anti-symmetric bifurcation dynamic buckling loads of rotationally restrained FG-GPLRC porous arches are derived by using an energy-based approach. Critical geometric parameters that determine the dynamic buckling mode switching behavior are also identified and discussed. Depending on the geometric parameters and the rotational restraint stiffness, the FG-GPLRC porous arch can buckle in either a symmetric limit point mode or an anti-symmetric bifurcation mode dynamically. It is also found that the dynamic buckling load of the arch can be considerably improved by adding a small amount of GPLs as reinforcing nanofillers. The influences of the porosity coefficients, GPL weight fractions, arch dimensions and geometries on the dynamic buckling behavior of rotationally restrained FG-GPLRC porous arches are comprehensively investigated through extensive parametric studies.

Keywords: Limit point dynamic buckling; Bifurcation dynamic buckling; Functionally graded porous arch; Graphene platelets; Uniform step loading; Analytical solutions.

1. Introduction

Lightweight materials and structures are of great significance due to their high cost-effectiveness, superior mechanical performance and associated environmental benefits [1-3]. Therefore, porous materials such as metal foams have been attracting considerable interests and attention from both research and industry communities [4, 5].

A vast number of research studies have been devoted to investigate the structural behavior of functionally graded (FG) porous structures. Magnucki and Stasiewicz [6] analyzed the elastic buckling behavior of a porous beam. Bahaadini et al. [7] performed the stability analysis of spinning thin-walled porous beams under a compressive axial load. Chen et al. [8, 9] carried out the buckling, bending and nonlinear free vibration analyses of FG porous beams. Jalaei et al. [10] studied the dynamic instability of magnetically embedded viscoelastic porous FG nanobeams and found that the porosity effect on the dynamic stability of FG nanobeams largely depends on the power-law index and magnetic fields. Gao et al. [11] presented the nonlinear primary resonance of FG porous cylindrical shells with multiscale method. Wu et al. [12, 13] investigated the free and forced vibration characteristics as well as the uncertain static behavior of FG porous structures through finite element method. In addition, She et al. [14, 15] further analyzed the snap-buckling and nonlinear bending behavior of FG porous curved nanotubes. Li and his co-workers presented the nonlinear vibration [16] and buckling [17, 18] analyses of porous beams and observed that the mechanical behavior of porous beams is directly related to its porosity distribution. Karami et al. investigated the free vibration of doubly-curved nanoshells [19] and porous nanotubes with variable thickness [20] according to a modified power law rule and the Hamiltonian principle. Fan et al. [21-23] conducted a series of studies on the buckling, thermal postbuckling, and nonlinear oscillations of porous FG micro/nano-plates via a non-uniform rational B-spline formulation.

Concurrent to the above studies, incorporating graphene nanoplatelets (GPLs) into matrix materials has recently been proven to be a highly effective way to enhance the mechanical performance of composite structures [24-27]. Rafiee et al. [28, 29] experimentally found that the Young' modulus, tensile strength and fracture toughness of nanocomposites can be remarkably improved by adding a small amount of GPLs, and the reinforcing effect is much better than using CNTs as reinforcing nanofillers. Liu et al. [30, 31] demonstrated that the mechanical properties of graphene reinforced alumina-ceramic composites are higher than those monolithic ceramic composites. In another experimental work, Tang et al. [32] reported that graphene reinforced nanocomposites possess higher strength and fracture toughness when graphene is highly dispersed in a polymer matrix. Furthermore, many researchers have conducted a series of studies on mechanical behavior of FG-GPLRC porous structures. For example, the free vibration, elastic buckling, post-

buckling and nonlinear bending of FG-GPLRC porous beams have been comprehensively investigated [33-35]. In addition, Li et al. [36] conducted the isogeometric analysis of FG-GPLRC porous plates. In addition to beam and plate structures, FG-GPLRC cylindrical shells have also been widely studied to reveal the characteristics of buckling [37], linear vibration [38] and nonlinear dynamics [39]. These results have shown that the prominent mechanical performance of porous materials and the excellent reinforcing effect of GPLs.

Arch structures have been widely implemented in mechanical and structural engineering due to its elegant shape and mechanical performance. It is often adopted as a major structural element to support the overall skeleton of structures. In real-engineering applications, arch structures are mainly subjected to dynamic loads such as wind and impact loads. Due to the compression and bending stress characteristics on arch structures, the dynamic behaviors become the main factors for the arch bearing capacity. Numerous research studying on dynamic stability and buckling of isotropic arch structures can be found in the open literature [40-47]. Considering an anisotropic composite arch, Yang et al. [48-53] discussed the free vibration, buckling and postbuckling characteristics of FG-GPLRC arches and found that the structural behavior of the FG-GPLRC arch is quite sensitive to boundary conditions and thermal effect. Liu et al. [54] investigated the nonlinear behavior and stability of FG-GPLRC arches under a static uniform load and verified the reinforcing effect of GPLs on the buckling load of FG-GPLRC arches. Li et al. [55, 56] further studied the coupling effects of thermal and mechanical loads on the stability of confined FG arches. Zhao et al. [57] investigated the free vibration, elastic buckling and dynamic instability of functionally graded porous arches reinforced by graphene platelets. However, no previous work has been reported on the dynamic buckling behavior of dynamically loaded FG-GPLRC porous arches under general boundary conditions, despite its practical significance.

Therefore, the purpose of this paper is to fill this important knowledge gap to gain, for the first time, an in-depth understanding of the dynamic buckling performance of such an arch subjected to a uniform step load. The effective materials properties of FG-GPLRC porous arches are determined by the volume fraction distribution of materials. Analytical solutions for the symmetric limit point dynamic buckling and anti-symmetric bifurcation dynamic buckling loads are obtained through an energy-based method for FG-GPLRC porous arch with elastically restrained ends which is a generic boundary condition model covering free, pinned, and fixed end boundary conditions. Effects of porosity coefficients, GPL weight fraction, elastic constraints, and geometrical parameters on the dynamic buckling characteristics of rotationally restrained FG-GPLRC porous arches are comprehensively studied. The critical parameters governing the switching dynamic buckling mode of the FG-GPLRC porous arch are discussed in detail.

2. Effective materials properties

The material properties of FG-GPLRC porous arches with a thickness of h and width of b are shown in Fig. 1. Two different porosity distributions with a uniform GPL reinforcement along the thickness direction are considered in this study. Noted that $E_{\max}$ and $E_{\min}$ are the maximum and minimum elastic moduli of the porous material, respectively.

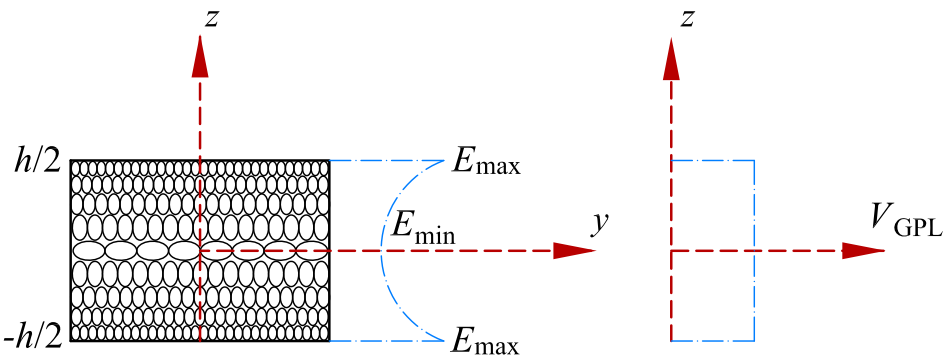

(a) Porosity distribution 1 with a uniform GPL distribution (PD1)

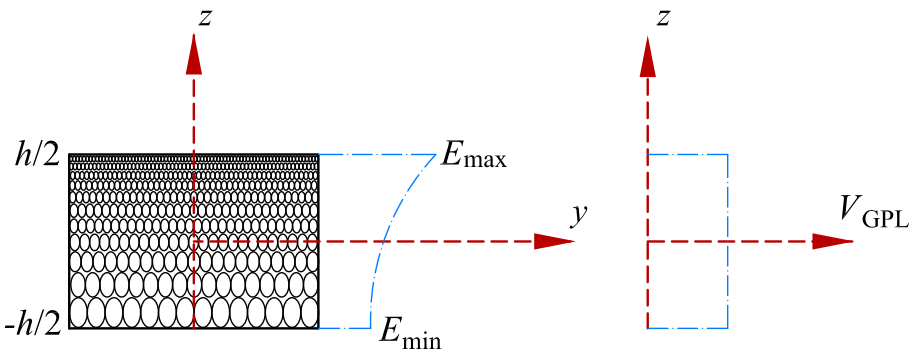

(b) Porosity distribution 2 with a uniform GPL distribution (PD2)

Fig. 1 Porosity distribution types

The elastic modulus and mass density of FG-GPLRC porous arches with the porosity distribution 1 (PD1) and porosity distribution 2 (PD2) are given as [54]

$$E(z)=E_c\left[1-e_0\xi(z)\right] \tag{1}$$

$$\rho(z)=\rho_c\left[1-e_m\xi(z)\right] \tag{2}$$

where e_0 is the porosity coefficient as defined by

$$e_0=1-\frac{E_{\min}}{E_{\max}} \tag{3}$$

According to the Gaussian random field scheme, the mechanical properties of the closed-cell cellular solids can be formulated as [34, 58]

$$\frac{E(z)}{E_c}=\left[\frac{1.121-e_m\xi(z)}{1.121}\right]^{2.3} \tag{4}$$

from which the mass density coefficient e_m can be derived as

$$e_m=\frac{1.121\left(1-\sqrt[2.3]{1-e_0\xi(z)}\right)}{\xi(z)} \tag{5}$$

where $\xi(z)$ is the distribution function of the aforementioned porosity distributions as shown in Fig. 2, which can be written as

$$\text{PD1:}\quad \xi(z)=\cos\left(\frac{\pi z}{h}\right) \tag{6}$$

$$\text{PD2:}\quad \xi(z)=\cos\left(\frac{\pi z}{2h}+\frac{\pi}{4}\right) \tag{7}$$

The effective Young's modulus E_c is determined by the Halpin–Tsai micromechanical model as [28, 48-53]

$$E_c=\frac{3\left(1+\xi_L\eta_L V_{GPL}\right)}{8\left(1-\eta_L V_{GPL}\right)}\times E_M+\frac{5\left(1+\xi_T\eta_T V_{GPL}\right)}{8\left(1-\eta_T V_{GPL}\right)}\times E_M \tag{8}$$

with

$$\eta_L=\frac{\left(E_{GPL}/E_M\right)-1}{\left(E_{GPL}/E_M\right)+\xi_L},\quad \eta_T=\frac{\left(E_{GPL}/E_M\right)-1}{\left(E_{GPL}/E_M\right)+\xi_T} \tag{9}$$

$$\xi_L=2\left(a_{GPL}/b_{GPL}\right)\times\xi_T/2,\quad \xi_T=2\left(b_{GPL}/t_{GPL}\right) \tag{10}$$

$$V_{GPL}=\frac{\rho_M W_{GPL}}{\rho_M W_{GPL}+\rho_{GPL}\left(1-W_{GPL}\right)} \tag{11}$$

where E_{GPL} and E_M are the Young's moduli of GPL nanofillers and metal matrix, respectively. a_{GPL}, b_{GPL}, t_{GPL}, a_{GPL}/b_{GPL} and b_{GPL}/t_{GPL} are the length, width, thickness, aspect ratio and width-to-thickness ratio of GPLs, respectively. V_{GPL} is the volume fraction of GPLs. W_{GPL} is the GPL weight fraction.

The mass density of the composite is given by the rule of mixture as

$$\rho_c=\rho_{GPL}V_{GPL}+\rho_M V_M \tag{12}$$

where ρ_{GPL} and ρ_M are the mass densities of GPLs and metal matrix, respectively. Note that the volume fractions V_M and V_{GPL} are related by $V_M+V_{GPL}=1$.

3. Equations of motion

A rotationally restrained FG-GPLRC porous arch, having a central angle 2Θ, radius R and arc length S, under a uniform step load is shown in Fig. 2. The stiffness of the elastic rotational constraints at both ends is k, and θ is the angular coordinate in the coordinate system.

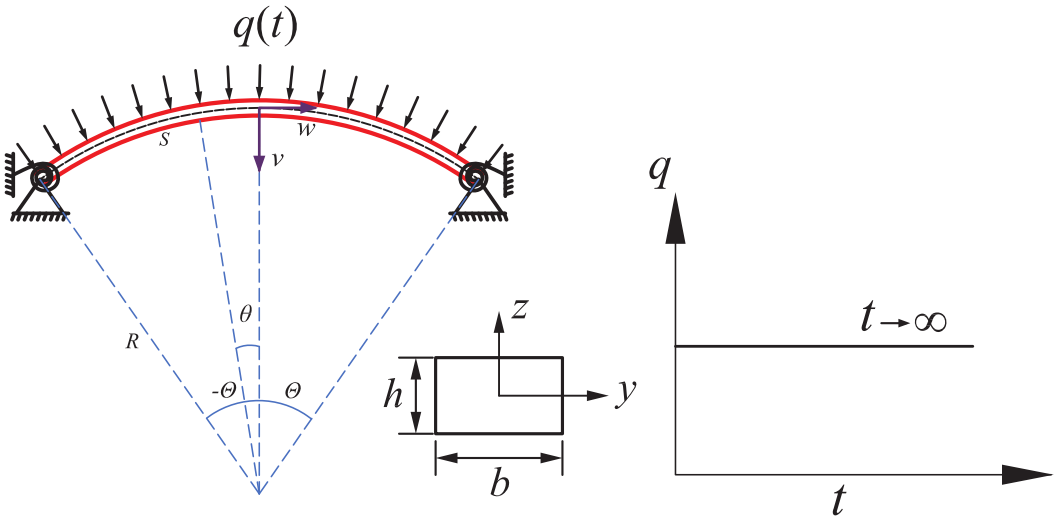

Fig. 2 Configuration and coordinate system of a FG-GPLRC porous arch under a uniform step load

It is assumed in the present analysis that (i) the FG-GPLRC porous arch is linearly elastic; (ii) the lateral and torsional deformations of the arch are fully restrained; and (iii) the damping effect is neglected in this study. According to the classical arch theory [48], the displacement fields of the arch are presented as

$$V(\theta,t)=v(\theta,t) \tag{13}$$

$$W(\theta,t)=w(\theta,t)-\frac{z}{R}v'(\theta,t) \tag{14}$$

where $(\,)'\equiv d(\,)/d\theta$, V and W are the displacements of the arch along z and y directions, respectively; v and w are the mid-plane (z = 0) displacements of the arch in the z and y directions, respectively. Accordingly, the nonlinear strain-displacement relations are derived from the above displacement field as

$$\varepsilon=\tilde{w}'-\tilde{v}+\frac{\tilde{v}'^2}{2}-\frac{z}{R}\tilde{v}'' \tag{15}$$

in which $\tilde{v}=v/R$ and $\tilde{w}=w/R$ are the dimensionless radial and axial displacements, respectively.

The governing equations of the rotationally restrained FG-GPLRC porous arch can be derived by using the Hamilton's principle given as

$$\int_{t_1}^{t_2}\delta(T-U)\,dt=0 \tag{16}$$

with $\delta\tilde{v}=\delta\tilde{w}=0$ at $t=t_1, t_2$ for $-\Theta\le\theta\le\Theta$. The kinetic energy T and total potential energy U are derived as

$$T=\frac{1}{2}\int_{-\Theta}^{\Theta}Rb\int_{-h/2}^{h/2}\rho(z)\left[\left(\frac{\partial V}{\partial t}\right)^2+\left(\frac{\partial W}{\partial t}\right)^2\right]dzd\theta \tag{17}$$

$$U=\frac{1}{2}\int_{-\Theta}^{\Theta}Rb\int_{-h/2}^{h/2}E(z)\varepsilon^2\,dzd\theta-\int_{-\Theta}^{\Theta}qR^2\tilde{v}\,d\theta+\frac{1}{2}\sum_{i=\pm\Theta}k\tilde{v}_i'^2 \tag{18}$$

Substituting Eqs. (13), (14), (15), (17) and (18) into Eq. (16), and setting the coefficients of $\delta\tilde{v}$ and $\delta\tilde{w}$ in Eq. (16) to be zero, the governing equations of the arch can be derived as

$$(NR)'=I_0\ddot{w}-\frac{I_1}{R}\ddot{v}' \tag{19}$$

$$NR+(NR\tilde{v}')'-M''-qR^2=I_0\ddot{v}-\frac{I_1}{R}\ddot{w}+\frac{I_2}{R}\ddot{v}' \tag{20}$$

where

$$N=-A_{11}\left(\tilde{w}'-\tilde{v}+\frac{\tilde{v}'^2}{2}\right)+\frac{B_{11}}{R}\tilde{v}''\quad\text{(Axial compressive force)} \tag{21}$$

$$M=B_{11}\left(\tilde{w}'-\tilde{v}+\frac{\tilde{v}'^2}{2}\right)-\frac{D_{11}}{R}\tilde{v}''\quad\text{(Bending moment)} \tag{22}$$

and the inertia related terms and the stiffness components are given by

$$\{I_0,I_1,I_2\}=b\int_{-h/2}^{h/2}\rho(z)\{1,z,z^2\}\,\mathrm{dz} \tag{23}$$

$$\{A_{11},B_{11},D_{11}\}=b\int_{-h/2}^{h/2}E(z)\{1,z,z^2\}\,\mathrm{dz} \tag{24}$$

In this analysis, the FG-GPLRC porous arch with elastic rotational constraints at both ends is considered, and the associated boundary conditions are

$$\tilde{v}=\tilde{w}=0,\ -M_{\pm\Theta}\pm k\tilde{v}'_{\pm\Theta}=0\quad\text{at}\quad\theta=\pm\Theta \tag{25}$$

and the initial conditions at $t = 0$ are assumed to be

$$\tilde{v}=\tilde{w}=0\quad\text{and}\quad\dot{\tilde{v}}=\dot{\tilde{w}}=0 \tag{26}$$

where the dot over $\tilde{v}$ and $\tilde{w}$ denotes differentiation with respect to t.

4. Nonlinear equilibrium

4.1 Limit point equilibrium

When the FG-GPLRC porous arch is subjected to a static uniform load q, the inertia terms in Eqs. (19) and (20) are neglected, the equilibrium and stability equations of the arch can be obtained as

$$\left(NR\right)' = 0 \tag{27}$$

$$NR + \left(NR\tilde{v}'\right)' - M'' - qR^2 = 0 \tag{28}$$

Substituting Eqs. (21), (22) and (27) into Eq. (28) yields the following fourth-order differential equation in the radial direction of the arch as follows

$$\frac{\tilde{v}^{iv}}{\mu^2} + \tilde{v}'' = P \tag{29}$$

where μ is the dimensionless axial force parameter defined by

$$\mu^2 = \frac{NR^2}{\kappa} \quad \text{with} \quad \kappa = D_{11} - \frac{B_{11}^2}{A_{11}} \tag{30}$$

and the dimensionless load P is defined by

$$P = \frac{qR - N}{N} \tag{31}$$

The dimensionless radial displacement $\tilde{v}$ can be obtained by solving Eq. (29) in conjunction with the associated boundary conditions specified in Eq. (25) as

$$\tilde{v} = \frac{P}{\mu^2}\left[\left(\cos\beta - \cos\mu\theta\right)\beta K_1 + \frac{1}{2}\left(\mu^2\theta^2 - \beta^2\right)\right] - \frac{B\left(\cos\beta - \cos\mu\theta\right)K_2}{R} \tag{32}$$

with $B = B_{11}/A_{11}$, $\beta = \mu\Theta$, α is the relative flexibility of the elastic rotational constraints defined as $\alpha = \kappa/kS$. The parameters K_1 and K_2 are given by

$$K_1 = -\frac{2\alpha + 1}{2\alpha\beta\cos\beta + \sin\beta}, \quad K_2 = \frac{2\alpha\beta}{2\alpha\beta\cos\beta + \sin\beta} \tag{33}$$

Substituting Eq. (32) into Eq. (21) gives the nonlinear relationship between the parameter β and the applied load P as

$$A_1P^2 + B_1P + C_1 = 0 \tag{34}$$

with

$$A_1 = \frac{\beta - \sin\beta\cos\beta}{4\beta}K_1^2 + \frac{\sin\beta - \beta\cos\beta}{\beta^2}K_1 + \frac{1}{6} \tag{35}$$

$$B_1 = \frac{\sin\beta - \beta\cos\beta}{\beta^2}K_1 + \frac{1}{3} + \frac{B_0K_2}{\lambda}\left(\frac{\beta\cos\beta - \sin\beta}{\beta} - \frac{\beta - \sin\beta\cos\beta}{2}K_1\right) - \frac{B_0\left(K_1\sin\beta + 1\right)}{\lambda} \tag{36}$$

$$C_1 = \frac{\beta^2 r_{11}^2}{\lambda^2} + \frac{B_0^2\beta K_2}{\lambda^2}\frac{\left(4 - K_2\cos\beta\right)\sin\beta + K_2\beta}{4} + \frac{B_0K_2\left(\beta\cos\beta - \sin\beta\right)}{\lambda\beta} \tag{37}$$

where $B_0 = B/h$ and $r_{11} = \sqrt{\kappa / A_{11}}/h$. λ is the arch geometrical parameter as given by

$$\lambda = \frac{R\Theta^2}{h} = \frac{S}{h}\frac{\Theta}{2} \tag{38}$$

When a uniform radial load is applied to the FG-GPLRC porous arch, the arch may buckle in a symmetric limit point instability mode. The limit point loads may be either maxima or minima on the nonlinear equilibrium path and can be found from

$$A_2 P^2 + B_2 P + C_2 = 0 \tag{39}$$

with

$$A_2 = \frac{\beta \partial A_1}{\partial \beta} - 4A_1, \quad B_2 = -4A_1 + \frac{\beta \partial B_1}{\partial \beta} - 2B_1, \quad C_2 = -2B_1 + \frac{\beta \partial C_1}{\partial \beta} \tag{40}$$

By solving Eqs. (34) and (39), combining Eq. (32), the solutions of the limit point load and limit point equilibrium path of FG-GPLRC porous arches under a uniform radial load can be determined.

4.2 Bifurcation equilibrium

The FG-GPLRC porous arch with with elastic rotational constraints may also buckle in an anti-symmetry bifurcation mode. The critical condition for equilibrium may be stated that the second variation of the total potential of the arch system is equal to zero for any admissible infinitesimal variations of the deformation. Thus, the differential equation for bifurcation buckling is [45]

$$\frac{\partial^4 w_b}{\mu^2} + w_b = 0 \tag{41}$$

The general solution of Eq. (41) is

$$w_b = E_1 + E_2\theta + E_3 \sin(\mu\theta) + E_4 \cos(\mu\theta) \tag{42}$$

where E_1, E_2, E_3 and E_4 are the undetermined coefficients.

$$w_b = \psi_b = 0, \quad \frac{\kappa \psi_b}{R} + k w_b = 0 \quad \text{at} \quad \theta = \pm\Theta \tag{43}$$

Substituting Eq. (43) into Eq. (42) obtains

$$\begin{bmatrix} 1 & -\Theta & -\sin\beta & \cos\beta \\ 1 & \Theta & \sin\beta & \cos\beta \\ 0 & 1 & -2\mu\alpha\beta\sin\beta + \mu\cos\beta & -2\mu\alpha\beta\cos\beta - \mu\sin\beta \\ 0 & -1 & 2\mu\alpha\beta\sin\beta - \mu\cos\beta & -2\mu\alpha\beta\cos\beta - \mu\sin\beta \end{bmatrix} \begin{Bmatrix} E_1 \\ E_2 \\ E_3 \\ E_4 \end{Bmatrix} = \begin{Bmatrix} 0 \\ 0 \\ 0 \\ 0 \end{Bmatrix} \tag{44}$$

To obtain the non-trivial solution for the coefficients E_1, E_2, E_3, and E_4, the determinant of the coefficient matrix must be zero, which leads to the characteristic equation as follows

$$\left[\frac{\sin\beta}{2\alpha}+\beta^2\left(\sin\beta-\frac{\cos\beta}{2\alpha\beta}\right)\right]\left(\cos\beta+\frac{\sin\beta}{2\alpha\beta}\right)=0 \tag{45}$$

The critical dimensionless axial force parameter β_b for the bifurcation buckling of FG-GPLRC porous arches can be obtained when the first factor of Eq. (45) vanishes and leads to

$$\beta_b=\eta_b\pi=\mu_b\Theta \tag{46}$$

Substituting Eq. (46) into Eq. (30), the axial compressive force N_a of the FG-GPLRC porous arch with elastic rotational constraints corresponding to an anti-symmetric buckling is obtained as

$$N_b=\frac{\mu_b^2\kappa}{R^2}=\frac{\left(\eta_b\pi\right)^2\kappa}{\left(S/2\right)^2} \tag{47}$$

The bifurcation equilibrium condition of the arch can be determined from the following equation by substituting Eq. (46) into Eq. (34) as

$$A_3P^2+B_3P+C_3=0 \tag{48}$$

with

$$A_3=A_{1,\,\beta=\eta_b\pi},\quad B_3=B_{1,\,\beta=\eta_b\pi},\quad C_3=C_{1,\,\beta=\eta_b\pi} \tag{49}$$

from which the bifurcation load is solved as

$$P=\frac{-B_3\pm\sqrt{B_3^2-4A_3C_3}}{2A_3} \tag{50}$$

The existence of real solutions in Eq. (50) requires $B_3^2-4A_3C_3\geq 0$, which gives a critical geometric parameter λ_{b1} that triggers the bifurcation buckling of the arch. At the bifurcation point, the arch bifurcates from its primary equilibrium path to the bifurcation equilibrium path which can be found by assuming its postbuckling displacement $\tilde{v}_t$ as [59]

$$\tilde{v}_t=\tilde{v}_s+\tilde{v}_a \tag{51}$$

where $\tilde{v}_s$ is the symmetric component of the displacement as follows

$$\tilde{v}_s=\frac{P}{\mu_b^2}\left[\left(\cos\beta_b-\cos\mu_b\theta\right)\beta_bK_1+\frac{1}{2}\left(\mu_b^2\theta^2-\beta_b^2\right)\right]-\frac{B\left(\cos\beta_b-\cos\mu_b\theta\right)K_2}{R} \tag{52}$$

and $\tilde{v}_a$ is the anti-symmetric component given as

$$\tilde{v}_a=\frac{K}{\mu_b^2}\left[\frac{\sin\left(\mu_b\theta\right)}{\cos\left(\mu_b\Theta\right)}-\frac{\mu_b\theta}{1+2\alpha\mu_b^2\Theta^2}\right] \tag{53}$$

where the amplitude parameter K can be solved by substitution of Eq. (51) into Eq. (21) then

integration of Eq. (21) along the arch length as

$$A_4P^2 + B_4P + C_4 + D_4K^2 = 0 \tag{54}$$

with

$$A_4 = A_3,\ \ B_4 = B_3,\ \ C_4 = C_3 \tag{55}$$

and D_4 is

$$D_4 = \frac{2\beta_b \cos\beta_b + \left(4\alpha^2\beta_b^4 - 4\alpha\beta_b^2 - 3\right)\sin\beta_b}{4\beta_b^3\left(2\alpha\beta_b^2 + 1\right)^2\cos\beta_b} + \frac{1}{4\beta_b^2\cos^2\beta_b} \tag{56}$$

The bifurcation equilibrium path can then be determined by combining Eqs. (51) and (54). The amplitude parameter K can be solved from Eq. (54) as follows

$$K = \pm\sqrt{\frac{A_4P^2 + B_4P + C_4}{-D_4}} \tag{57}$$

5. Dynamic buckling analysis

5.1 Dynamic buckling load

Under a small step load, the FG-GPLRC porous arch oscillates about its equilibrium position and does not enter into its unstable equilibrium path. Once the applied load is sufficiently large such that the arch reaches its unstable equilibrium path, dynamic buckling will occur. The energy-based method is employed in this section to derive the dynamic buckling load. For a conservative system, the total energy $\overline{\Pi}$ of the arch remains constant

$$\overline{\Pi} = \overline{U} + \overline{T} = \text{constant} \tag{58}$$

Substituting Eqs. (21) and (22) into Eqs. (17) and (18) and dividing by κ/R, respectively, the dimensionless kinetic energy $\overline{T}$ and total potential energy $\overline{U}$ can be expressed as

$$\overline{T} = \frac{R^2 b}{2\kappa}\int_{-\Theta}^{\Theta}\int_{-h/2}^{h/2}\rho(z)\left[\left(\frac{\partial V}{\partial t}\right)^2 + \left(\frac{\partial W}{\partial t}\right)^2\right]dzd\theta \tag{59}$$

$$\overline{U} = \frac{r_{11}^2\beta^5}{\mu\lambda^2} + \int_{-\Theta}^{\Theta}\left(\frac{\tilde{v}''^2}{2} - \frac{qR^3\tilde{v}}{\kappa}\right)d\theta + \frac{1}{4\alpha\Theta}\sum_{i=\pm\Theta}\tilde{v}_i'^2 \tag{60}$$

It is noted that the arch is initially at rest before the step load is applied. Herein, the total energy of the system is equal to zero, that is $\overline{\Pi} = \overline{U} + \overline{T} = 0$. Since the dimensionless kinetic energy $\overline{T}$ is always positive, the total energy $\overline{\Pi} = 0$ is true only when the dimensionless total potential energy $\overline{U} \le 0$. In other words, the condition for the oscillation to occur is $\overline{U} \le 0$, and its critical state is

$$\overline{U} = 0 \tag{61}$$

As previously discussed, the FG-GPLRC arch may buckle in either a limit point instability mode or a bifurcation mode. When a limit point buckling occurs, substitution of Eq. (32) into Eq. (60) gives the dimensionless total potential energy $\bar{U}$ as follows

$$\bar{U} = \Theta\left(A_5 P^2 + B_5 P + C_5\right) \tag{62}$$

with

$$\begin{aligned} A_5 = {} & \frac{\alpha\beta\left(\sin\beta\cos\beta+\beta\right)+\sin^2\beta}{2\alpha} K_1^2 + 2K_1\left(2\sin\beta-\beta\cos\beta\right) \\ & + \frac{K_1\sin\beta}{\alpha} + \frac{4\alpha\beta^2+6\alpha+3}{6\alpha} \end{aligned} \tag{63}$$

$$\begin{aligned} B_5 = {} & 2K_1\left(\sin\beta-\beta\cos\beta\right) + \frac{2\beta^2}{3} - \frac{\mu^2 B K_2}{R}\left[\frac{4\alpha\sin\beta-2\alpha\beta\cos\beta+\sin\beta}{\alpha\beta}\right. \\ & \left. + \frac{\left(\alpha\beta\cos\beta\sin\beta+\alpha\beta^2+\sin^2\beta\right)K_1}{\alpha\beta}\right] \end{aligned} \tag{64}$$

$$C_5 = \frac{\beta^4 r_{11}^2}{\lambda^2} + \frac{\mu^4 B^2 K_2^2}{R^2}\left(\frac{\sin^2\beta}{2\alpha\beta^2} + \frac{\beta+\cos\beta\sin\beta}{2\beta}\right) + \frac{2\mu^2 B K_2\left(\beta\cos\beta-\sin\beta\right)}{R\beta} \tag{65}$$

For bifurcation buckling, the dimensionless total potential energy $\bar{U}$ can be derived by substituting Eq. (51) into Eq. (60) as

$$\bar{U} = \Theta\left(A_6 P^2 + B_6 P + C_6 + D_6 K^2\right) \tag{66}$$

with

$$A_6 = A_{5,\,\beta=\eta_b\pi}, \quad B_6 = B_{5,\,\beta=\eta_b\pi}, \quad C_6 = C_{5,\,\beta=\eta_b\pi} \tag{67}$$

and D_6 is

$$D_6 = \frac{2\alpha\beta_b^2}{\left(2\alpha\beta_b^2+1\right)^2} + \frac{\beta_b-\sin\beta_b\cos\beta_b}{2\beta_b\cos^2\beta_b} \tag{68}$$

The arch remains unbuckled and oscillates around its stable equilibrium position under a small step load but will move into an unstable equilibrium position and lose its in-plane stability in the dynamic buckling mode when the step load is large enough. Hence, another necessary condition for dynamic buckling to take place is that the oscillation of the arch induced by the step load needs to attain the unstable equilibrium position.

In what follows, an aluminum-based metal matrix with the material properties E_{M} = 70GPa and $\rho_{\mathrm{M}} = 2700\,\mathrm{kg/m^3}$ is chosen in the following study. The FG porous arch (b×h = 0.03m×0.025m) is reinforced by GPLs (E_{GPL} = 1010GPa, $\rho_{\mathrm{GPL}} = 1062.5\,\mathrm{kg/m^3}$, a_{GPL} = 2.5μm, b_{GPL} = 1.5μm and t_{GPL} = 1.5nm) uniformly dispersed in the metal matrix. For the limit point dynamic buckling, a rotationally restrained FG-GPLRC porous arch (PD2 pattern) for $\alpha = 0.02$ is investigated, and its limit point

dynamic buckling load is presented in Fig. 3, where v_c is the displacement of the arch crown; f is the rise of the arch. The solid line is the nonlinear equilibrium path calculated from Eqs. (32) and (34) in which "*ab*", "*bc*", and "*cd*" are the primary stable equilibrium path, unstable equilibrium path, and remote stable equilibrium path, respectively. The dash line represents the total potential energy $\overline{U}$ corresponding to the nonlinear equilibrium path obtained from Eq. (62). Noted that N_{b0} is the value of N_b of the aluminium-based metal arch.

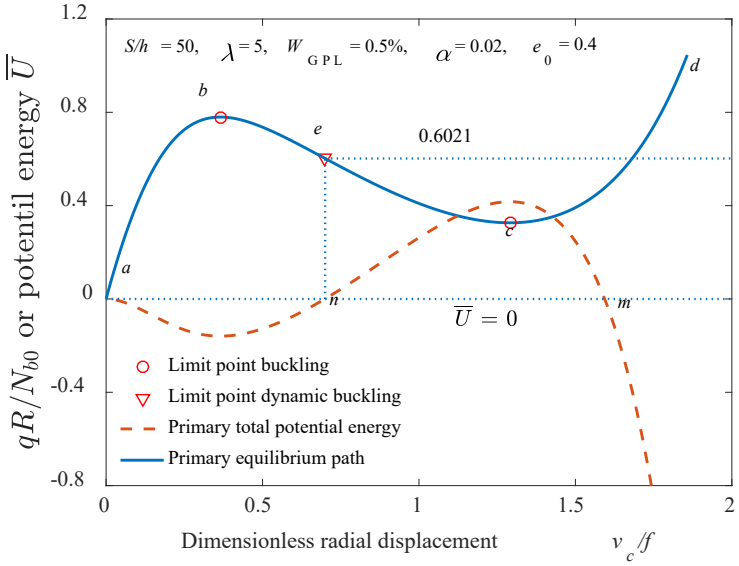

Fig. 3 Limit point dynamic buckling of an FG-GPLRC porous arch (PD2 pattern) for $\alpha = 0.02$

As shown in Fig. 3 that there exist two possible points (n and m) in the total potential energy curve at which $\overline{U} = 0$ and the arch may experience dynamic buckling under a uniform step load. At point m, its corresponding point on the nonlinear equilibrium path is located in the remote stable path "*cd*" and is a stable point where the arch does not buckle dynamically. However, at point n, its corresponding point e with $qR/N_{b0} = 0.6021$ on the nonlinear equilibrium path is located in the unstable equilibrium path *bc*. This means that under a uniform step load $qR/N_{b0} = 0.6021$, the arch will oscillate to the unstable equilibrium point e and lose its in-plane stability dynamically by snapping through from the unstable equilibrium point e to the remote stable path "*cd*". Hence, the limit point dynamic buckling load of the FG-GPLRC porous arch is determined to be 0.6021 in this loading case. Moreover, the limit point dynamic buckling load and the corresponding axial force can be determined by solving Eqs. (34) and (62) simultaneously as shown in Fig. 4.

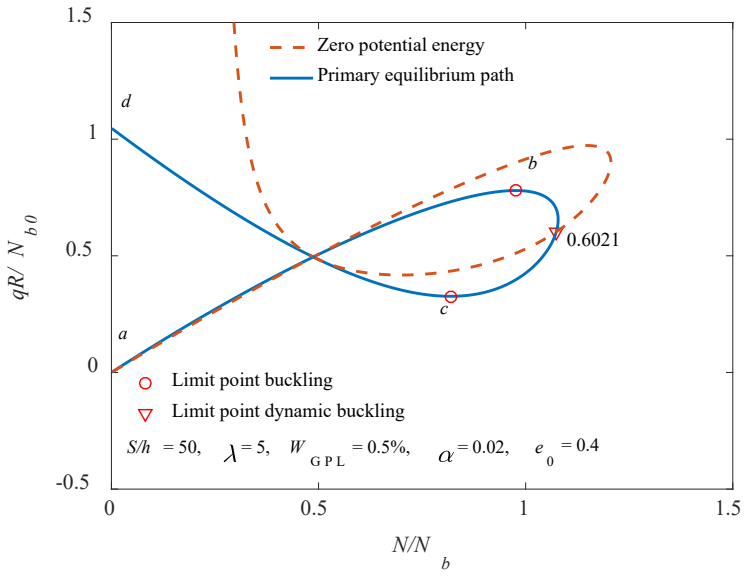

Fig. 4 Limit point dynamic buckling load of an FG-GPLRC porous arch (PD2 pattern) for $\alpha = 0.02$.

The behavior of anti-symmetric bifurcation dynamic buckling is depicted in Fig. 5 where the results of a rotationally restrained FG-GPLRC porous arch (PD2 pattern) for $\alpha = 0.5$ are presented. It is noted that the load increases along the primary stable equilibrium path *ab* (solid line) until the upper bifurcation point *g* is reached first and the arch buckles along the bifurcation unstable equilibrium path "*gh*" in an anti-symmetric mode. The potential energy corresponding to the bifurcation unstable equilibrium path "*gh*" is calculated by Eq. (66) and represented by a thick dash line. Note that the criterion in Eq. (61) is satisfied at point *o* only and its corresponding point in the nonlinear equilibrium path is point *s* with $qR/N_{b0} = 0.7137$ located on bifurcation unstable equilibrium path "*gh*". From the energy conservation principle, the oscillation of the arch under a uniform step load can reach the unstable equilibrium position *s* with zero kinetic energy, leading to an anti-symmetric bifurcation dynamic buckling which makes the arch jump to the remote equilibrium branch "*hd*". Hence, the uniform step load $qR/N_{b0} = 0.7137$ corresponding to the point *s* is defined as the bifurcation dynamic buckling load. It should be mentioned that this value can also be determined by solving Eqs. (54) and (66) simultaneously.

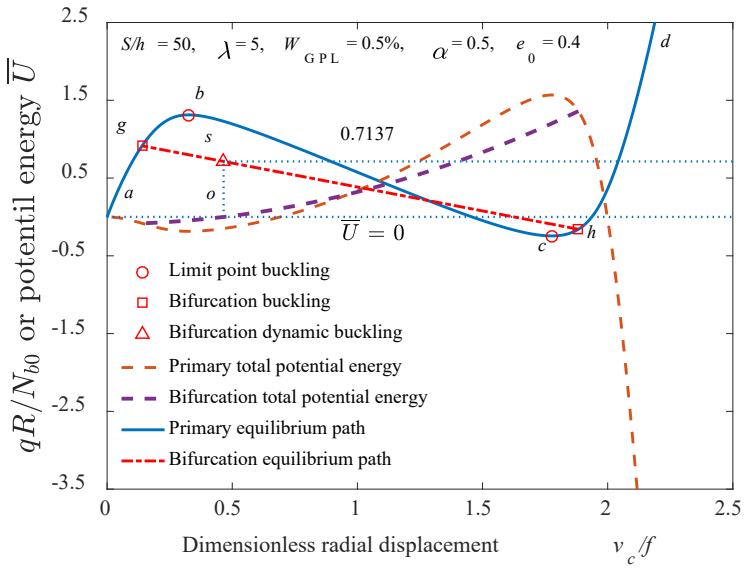

Fig. 5 Bifurcation dynamic buckling of an FG-GPLRC porous arch (PD2 pattern) for $\alpha = 0.5$

5.2 Dynamic buckling mode switching

As aforementioned, the bifurcation buckling of the FG-GPLRC porous arch may occur when $\lambda \geq \lambda_{b1}$. However, in some cases, the bifurcation point is located on the descending branch of the primary equilibrium path after the limit point buckling occurs, which means that the bifurcation point of the arch cannot be reached and the arch will buckle in a symmetric limit point instability mode. Hence, a critical geometric parameter λ_{b2} that defines the switching behavior between the symmetric limit point instability and anti-symmetric bifurcation buckling modes can be found by setting the symmetric limit point buckling load obtained from Eq. (39) to be equal to the anti-symmetric bifurcation buckling load obtained from Eq. (48) at $\beta = \beta_b$. When $\lambda \geq \lambda_{b2}$, the FG-GPLRC porous arch will buckle in an anti-symmetric bifurcation buckling mode.

On the other hand, a critical geometric parameter λ_s that defines the lowest dynamic buckling load of the FG-GPLRC porous arch can be determined by using the total potential energy approach as shown in Fig. 6. It can be seen that, when $\lambda > \lambda_s$, the total potential energy vanishes at two points: an unstable point and a stable point. The unstable point corresponds to the dynamic buckling point. However, when $\lambda < \lambda_s$, the total potential energy $\overline{U} < 0$, the arch motion cannot reach to its static equilibrium path and it just oscillates continuously without dynamic buckling.

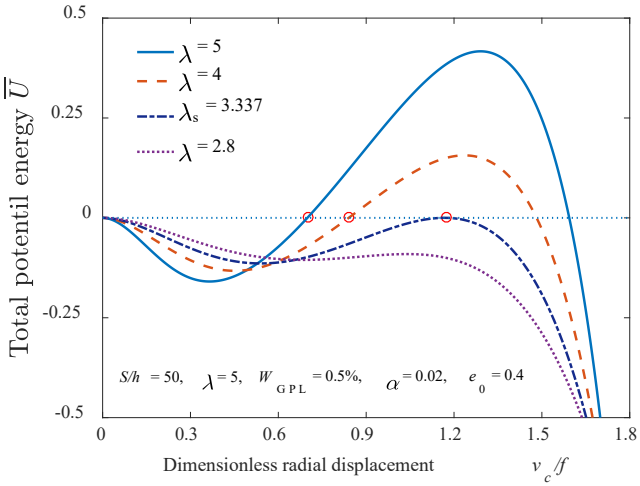

Fig. 6 Critical geometric parameter λ_s for the lowest dynamic buckling of an FG-GPLRC porous arch (PD2 pattern) for $\alpha = 0.02$

The effects of the flexibility of the elastic rotational constraints α on the critical geometric parameters (λ_{b2} , λ_{b1} and λ_s) of FG-GPLRC porous arches are shown in Fig. 7. It can be seen that, for both FG-GPLRC porous arches with the patterns PD1 and PD2, the critical geometric parameters increase with an increase of the rotational restraint stiffness. In region I ($\lambda > \lambda_{b2}$), the dynamic buckling of the FG-GPLRC porous arch is anti-symmetric bifurcation dynamic buckling; in region II ($\lambda_{b1} \le \lambda \le \lambda_{b2}$), the dynamic buckling of the FG-GPLRC porous arch is symmetric limit point dynamic buckling or anti-symmetric bifurcation dynamic buckling depending on which one occurs first; in region III ($\lambda_s \le \lambda < \lambda_{b1}$), the dynamic buckling of the FG-GPLRC porous arch is symmetric limit point dynamic buckling; and in region IV ($\lambda < \lambda_s$), the arch becomes a slightly curved beam and does not display dynamic buckling behavior but produces forced vibration under a uniform step load.

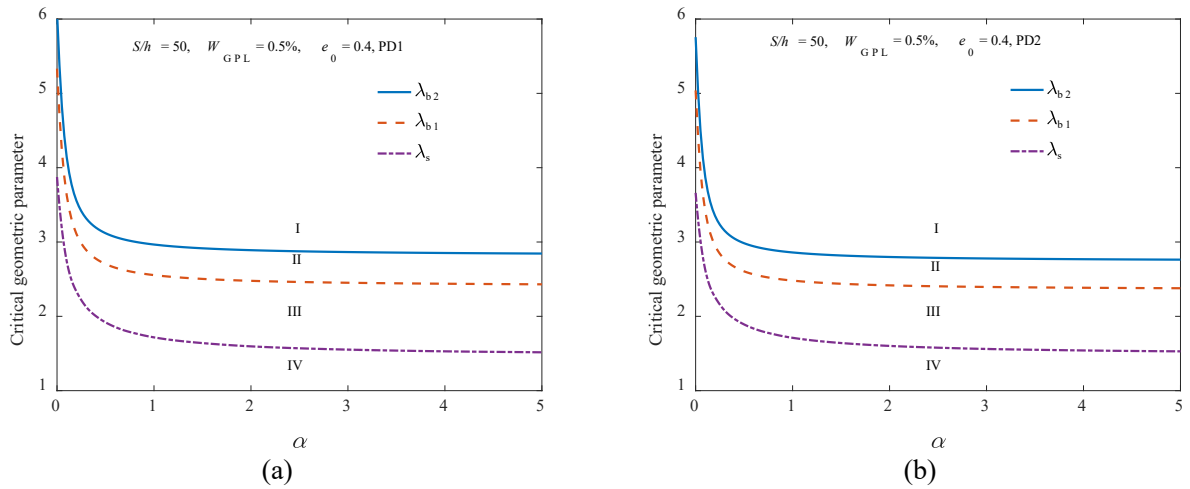

(a) (b)

Fig. 7 Critical geometric parameter for a rotationally restrained FG-GPLRC porous arch: (a) PD1 pattern; and (b) PD2 pattern

Table 1 shows the effects of the porosity on the critical geometric parameters of a rotationally restrained FG-GPLRC porous arch with $\alpha = 0.5$, in which $e_0 = 0$ stands for a solid arch. It is noted that the critical geometric parameters (λ_{b2} , λ_{b1} and λ_s) of the FG-GPLRC porous arch increase as the porosity increase, which means that the porosity has a significant contribution in the dynamic buckling mode switching of the FG-GPLRC porous arch.

Table 1 Critical geometric parameters of an FG-GPLRC porous arch (S/h = 50, W_{GPL} = 0.5%, $\alpha = 0.5$)

Distribution pattern	Critical geometric parameters	e_0			
		0	0.1	0.3	0.5
PD1	λ_{b2}	2.9377	2.9756	3.0651	3.1792
	λ_{b1}	2.5470	2.5799	2.6575	2.7564
	λ_s	1.4277	1.4462	1.4897	1.5452
PD2	λ_{b2}	2.9377	2.9503	2.9739	2.9906
	λ_{b1}	2.5470	2.5619	2.5915	2.6169
	λ_s	1.4277	1.4503	1.5007	1.5589

6. Results and discussion

6.1 Model verification

To validate the proposed analytical method for dynamic buckling loads of rotationally restrained FG-GPLRC porous arches, a finite element analysis (FEA) for the dynamic buckling is performed in this section by using the commercial software ANSYS 14.5 with elements SHELL181 and COMBIN14. To model the material variation, the cross section of the arch is subdivided into multiple layers in the thickness direction. The material properties are assigned to each layer according to Eqs. (1) and (2). Since it has been illustrated by the previous works [48, 53] that 10 individual layers are sufficiently accurate to model an ideal FG structure. Hence, 10 layers are adopted in the numerical verification for efficient computation but without compromising the accuracy of the results. The nonlinear transient dynamic analysis executed by ANSYS 14.5 is used to obtain the dynamic response of the arch subjected to a uniform step load. The FE results for a rotationally restrained FG-GPLRC porous arch (PD2 pattern) with $\alpha = 0.02$ under different step loads (i.e., qR/N_{b0} = 0.4817, 0.5900 and 0.6135) are plotted in Fig. 8a from which it can be seen that the arch motion is oscillatory under qR/N_{b0} = 0.4817 or 0.5900 but becomes so large that dynamic buckling occurs at qR/N_{b0} = 0.6135 which is very close to the analytical limit point dynamic buckling load $q_{cr}R/N_{b0}$ = 0.6021 obtained from Figs. 3 and 4. It can also be seen from Fig. 8b that the arch motion is symmetric, implying that the dynamic buckling of the FG-GPLRC porous arch for $\alpha = 0.02$ is a symmetric limit point dynamic buckling mode.

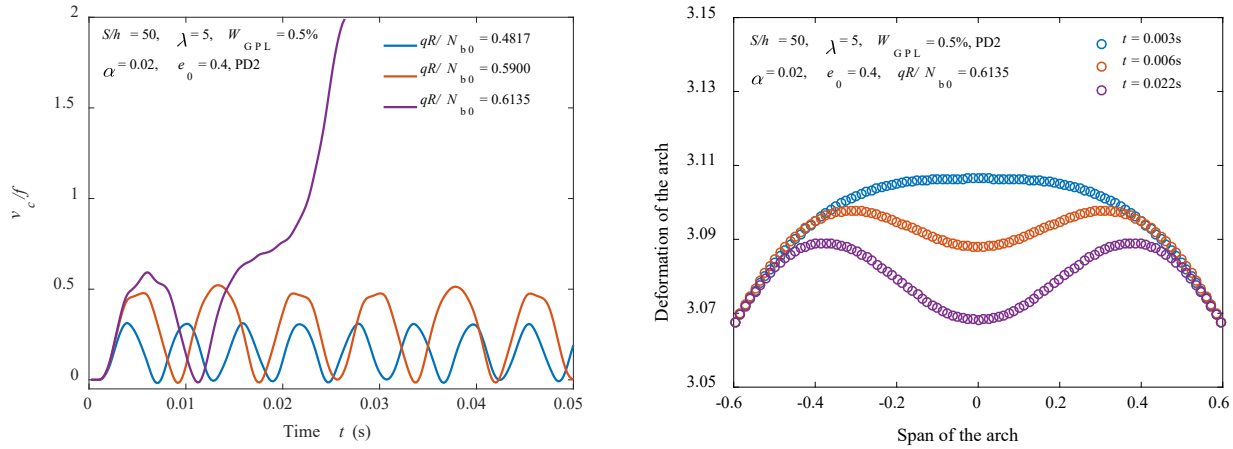

(a) (b)

Fig. 8 A rotationally restrained FG-GPLRC porous arch for $\alpha = 0.02$ under a uniform step load: (a) Transient responses under different load amplitudes; and (b) Deformed shapes of the arch at different time.

The transient responses of the rotationally restrained FG-GPLRC porous arch (PD2 pattern) for $\alpha = 0.5$ under the same step load are presented in Fig. 9a where the bifurcation dynamic buckling load can be determined in a similar way. It is worth noting that an anti-symmetric geometric imperfection of 0.1% arch length (S/1000) is introduced to trigger the anti-symmetric dynamic bifurcation behavior of the FG-GPLRC porous arch in FE analysis. Once again, the FE result ($q_{cr}R/N_{b0} = 0.7279$) agrees quite well with the analytical solution ($q_{cr}R/N_{b0} = 0.7137$). The deformed shapes of the arch shown in Fig. 9b indicate that the arch motion is anti-symmetric. Table 2 shows that the relative error between the present solutions and FE results is less than 2%, indicating that the analytical solutions agree well with the FE results.

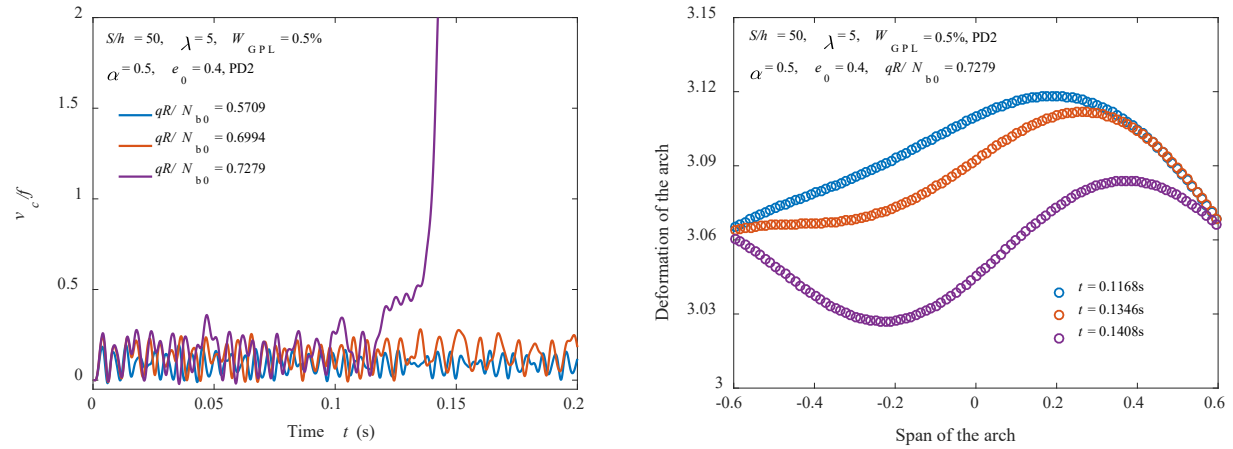

(a) (b)

Fig. 9 A rotationally restrained FG-GPLRC porous arch for $\alpha = 0.5$ under a uniform step load: (a) Transient responses under different load amplitudes; and (b) Deformed shapes of the arch at different time.

Table 2 Comparison of dynamic buckling load for an FG-GPLRC porous arch

Dynamic buckling load	Limit point	Bifurcation mode
Present solution	0.6021	0.7137
FE result	0.6135	0.7279
Relative error (%)	1.85%	1.95%

6.2 Parametric studies

The dynamic buckling load of rotationally restrained FG-GPLRC porous arches is studied in this section. The effects of the GPL weight fraction W_{GPL} and the porosity e_0 on the dynamic buckling load of FG-GPLRC porous arches with the patterns PD1 and PD2 are shown in Fig. 10 for symmetry limit point dynamic buckling, and in Fig. 11 for anti-symmetry bifurcation dynamic buckling. The following parameters are adopted for both buckling studies in Fig. 10 and Fig. 11 as: S/h = 50, h = 0.025m, and $\lambda = 5$. The flexibility of the elastic rotational constraints of the arch is adopted as $\alpha = 0.02$ for a limit point dynamic buckling study, and $\alpha = 0.5$ for a bifurcation dynamic buckling study. It is noted that the increase of the porosity e_0 reduces the dynamic buckling load of the FG-GPLRC porous arch at all specific W_{GPL}. On the other hand, the dynamic buckling load significantly increase by introducing the GPLs composites, and both dynamic buckling loads increase as GPL weight fraction W_{GPL} increases. Furthermore, the influences of the porosity and the GPLs reinforcement can be well illustrated by using the analytical equations. For example in Fig. 10a, by comparing to the solid arch (e_0 = 0) without GPLs reinforcement, the limit point dynamic buckling load is increased by 32.8% when adding 1% GPLs, but reduced over 30% when introducing a porosity level of 0.6. Furthermore, with the porosity introduced, the dimensionless mass $I_0/\rho_M bh$ of the FG-GPLRC porous arch decreases with the increasing of porosity e_0, as shown in Fig. 12.

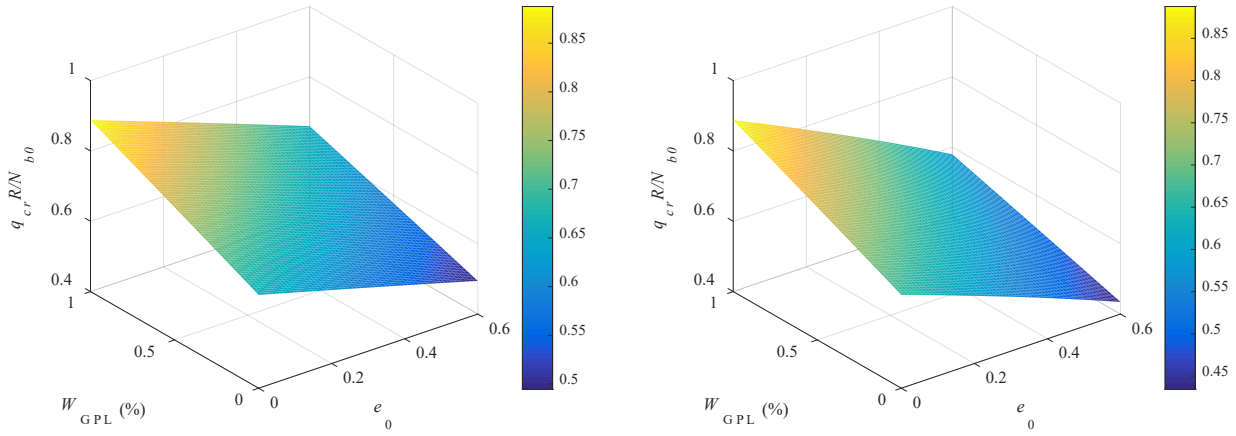

(a) (b)

Fig. 10 Effects of the GPL weight fraction W_{GPL} and the porosity e_0 on the limit point dynamic buckling load of an FG-GPLRC porous arch: (a) PD1 pattern; and (b) PD2 pattern

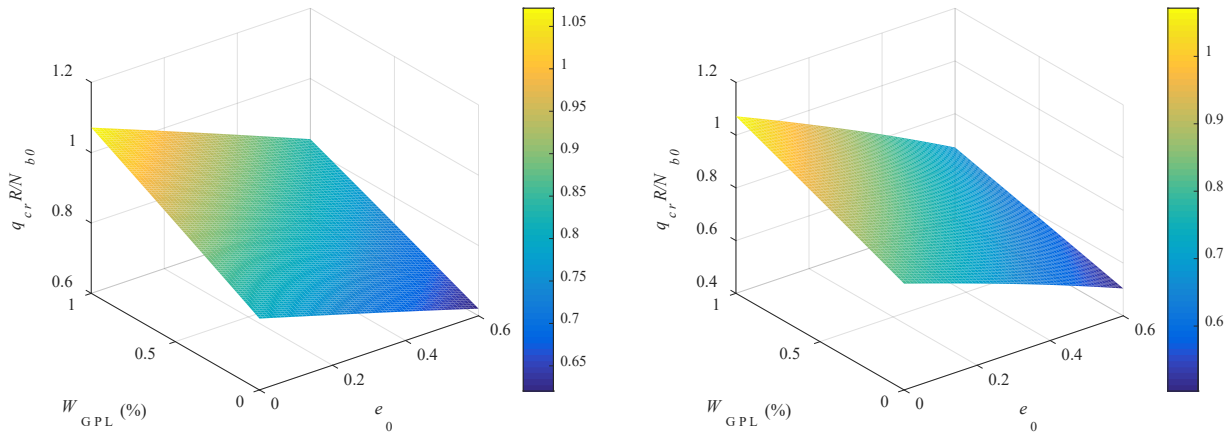

Fig. 11 Effects of the GPL weight fraction W_{GPL} and the porosity e_0 on the bifurcation dynamic buckling load of an FG-GPLRC porous arch: (a) PD1 pattern; and (b) PD2 pattern

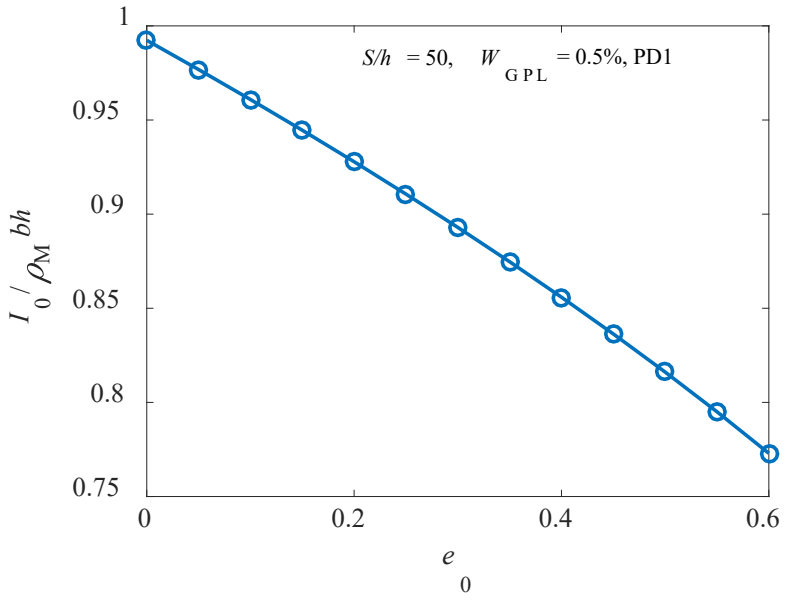

Fig. 12 Effect of porosity e_0 on the mass of an FG-GPLRC porous arch

The effect of GPL geometrical size is studied for the limit point dynamic buckling load of the FG-GPLRC porous arch (PD2 pattern) for $\alpha = 0.02$ in Fig. 13a, while for the bifurcation dynamic buckling load of the FG-GPLRC porous arch (PD1 pattern) for $\alpha = 0.5$ in Fig. 13b. As shown in these figures, the dynamic buckling load of the arch increases as the GPL width-to-thickness ratio and aspect ratio increase. The former effect is more significant than that of the latter one. This is because GPLs with a larger surface area and fewer single layers offer better enhancing effect on the effective Young's modulus of the GPL reinforced porous composites according to Eq. (8). Moreover, the influence of GPL geometry tends to be less pronounced when b_{GPL}/t_{GPL} is close to 10^3, beyond which the dynamic buckling load remains almost unchanged.

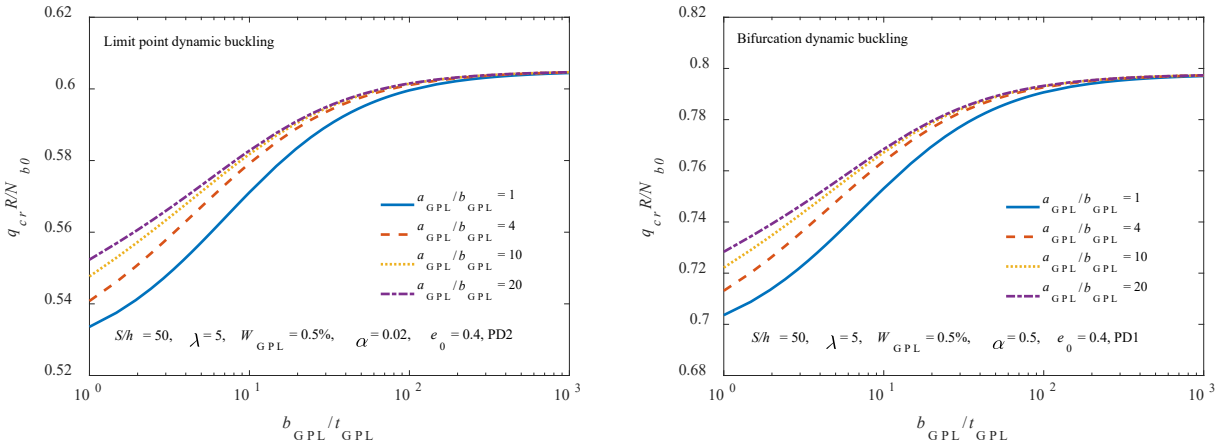

(a) (b)

Fig. 13 Effects of the GPL geometrical size on a rotationally restrained FG-GPLRC porous arch: (a) Limit point dynamic buckling load; and (b) Bifurcation dynamic buckling load

Fig. 14 shows the influence of the geometric parameter λ on the dynamic buckling load. It can be seen that the dynamic buckling load of the FG-GPLRC porous arch in both buckling modes becomes larger as λ increases. According to the critical geometric parameters shown in Fig. 7 and Table 1, for a very shallow arch having $1.7170 \le \lambda \le 2.9659$, the limit point buckling is the dominant mode and the arch will buckle in a limit point mode dynamically. When $\lambda > 2.9659$, the anti-symmetric bifurcation buckling mode becomes dominant and the arch will buckle in a bifurcation mode dynamically.

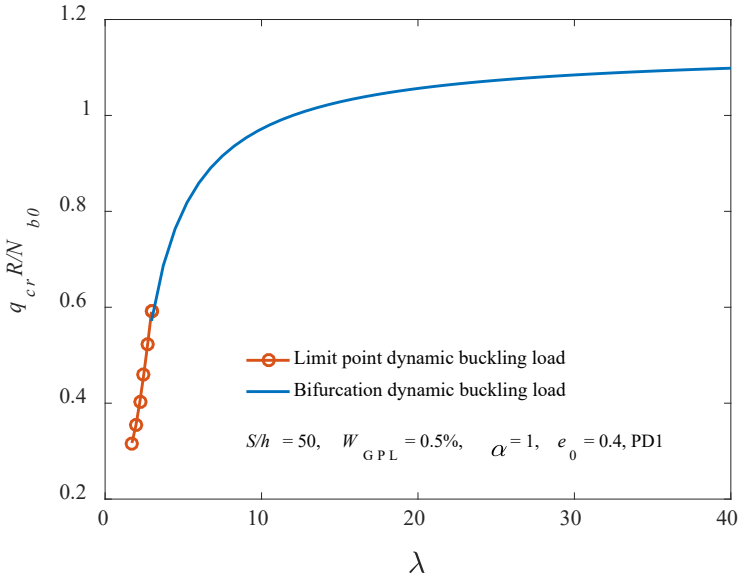

Fig. 14 Effect of the arch geometric parameter λ on the dynamic buckling load of an FG-GPLRC porous arch

7. Conclusions

The dynamic buckling behavior of rotationally restrained FG-GPLRC porous arches under a uniform step load has been investigated in this paper. Theoretical solutions for both symmetric limit

point and anti-symmetric bifurcation dynamic loads have been derived for rotationally restrained FG-GPLRC porous arches. The influences of porosity, GPL weight fraction, structural dimensions as well as arch geometries on the dynamic buckling behavior have been discussed in detail. It is found that the dynamic buckling load of the arch can be remarkably enhanced with the addition of a low content of GPLs. However, the dynamic buckling load is reduced as the porosity increases. Numerical results also showed that GPLs with a larger surface area and fewer single layers are preferred reinforcing nanofillers. The FG-GPLRC porous arch supported by elastic rotational constraints at both ends can buckle in either a symmetric limit point mode or an anti-symmetric bifurcation mode dynamically, depending on the geometric parameters and elastic rotational constraints. It should be noted that without the analytical solutions developed herein, the mechanism governing the dynamic buckling mode switching behavior of the FG-GPLRC porous arch by its material and geometry parameters cannot be easily predicted and well understood.

Acknowledgments

This research is financially supported by the National Natural Science Foundation of China (Nos. 51925802, 11972123, 51878188), Technology Planning Project of Guangdong Province (No. 2020A1414010319), China-Australia Joint Research Centre for Resilient Material and Structures (No. 2020A050519002), the Research Grants Council of Hong Kong through the General Research Fund (Project No. PolyU 152008/19E) and the Research Impact Fund (Project No. R5020-18), and the Australian Research Council Discovery Projects (DP210103656). The authors are grateful for these supports.

References

[1] Y. Feng, D. Wu, L. Liu, W. Gao, F. Tin-Loi, Safety assessment for functionally graded structures with material nonlinearity, Struct. Saf. 86 (2020) 101974.

[2] Q. Li, D. Wu, W. Gao, F. Tin-Loi, Size-dependent instability of organic solar cell resting on Winkler-Pasternak elastic foundation based on the modified strain gradient theory, Int. J. Mech. Sci. 177 (2020) 105306.

[3] Q. Li, D. Wu, W. Gao, F. Tin-Loi, Z. Liu, J. Cheng, Static bending and free vibration of organic solar cell resting on Winkler-Pasternak elastic foundation through the modified strain gradient theory, Eur. J. Mech. A-Solid 78 (2019) 103852.

[4] J. Banhart, Manufacture, characterisation and application of cellular metals and metal foams, Prog. Mater. Sci. 46 (2001) 559-632.

[5] H. Wu, J. Yang, S. Kitipornchai, Mechanical Analysis of Functionally Graded Porous Structures: A Review, Int. J. Struct. Stab. Dy. 20 (2020) 2041015.

[6] K. Magnucki, P. Stasiewicz, Elastic buckling of a porous beam, J. Theor. App. Mech-Pol. 42 (2004) 859-868.

[7] R. Bahaadini, A. R. Saidi, On the stability of spinning thin-walled porous beams, Thin Wall. Struct. 132 (2018) 604-615.

[8] D. Chen, J. Yang, S. Kitipornchai, Elastic buckling and static bending of shear deformable functionally graded porous beam, Compos. Struct. 133 (2015) 54-61.

[9] D. Chen, S. Kitipornchai, J. Yang, Nonlinear free vibration of shear deformable sandwich beam with a functionally graded porous core, Thin Wall. Struct. 107 (2016) 39-48.

[10] M. H. Jalaei, Ö. Civalek, On dynamic instability of magnetically embedded viscoelastic porous FG nanobeam, Int. J. Eng. Sci. 143 (2019), 14-32.

[11] K. Gao, W. Gao, B. Wu, D. Wu, C. Song, Nonlinear primary resonance of functionally graded porous cylindrical shells using the method of multiple scales, Thin Wall. Struct. 125 (2018) 281-293.

[12] D. Wu, A. Liu, Y. Huang, Y. Huang, Y. Pi, W. Gao, Mathematical programming approach for uncertain linear elastic analysis of functionally graded porous structures with interval parameters, Compos. Part B-Eng. 152 (2018) 282-291.

[13] D. Wu, A. Liu, Y. Huang, Y. Huang, Y. Pi, W. Gao, Dynamic analysis of functionally graded porous structures through finite element analysis, Eng. Struct. 165 (2018) 287-301.

[14] G. L. She, Y. R. Ren, K. M. Yan, On snap-buckling of porous FG curved nanobeams, Acta Astronaut. 161 (2019) 475-484.

[15] G. L. She, F. G. Yuan, B. Karami, Y. R. Ren, W. S. Xiao, On nonlinear bending behavior of FG porous curved nanotubes, Int. J. Eng. Sci. 135 (2019) 58-74.

[16] L. Li, H. Tang, Y. Hu, Size-dependent nonlinear vibration of beam-type porous materials with an initial geometrical curvature, Compos. Struct. 184 (2018) 1177-1188.

[17] B. Karami, D. Shahsavari, S. M. R. Nazemosadat, L. Li, A. Ebrahimi, Thermal buckling of smart porous functionally graded nanobeam rested on Kerr foundation, Steel Compos. Struct. 29 (2018) 349-362.

[18] H. Tang, L. Li, Y. Hu, Buckling analysis of two-directionally porous beam, Aerosp. Sci. Technol. 78 (2018) 471-479.

[19] B. Karami, D. Shahsavari, M. Janghorban, On the dynamics of porous doubly-curved nanoshells, Int. J. Eng. Sci., 143 (2019) 39-55.

[20] B. Karami, M. Janghorban, On the dynamics of porous nanotubes with variable material properties and variable thickness, Int. J. Eng. Sci. 136 (2019) 53-66.

[21] F. Fan, B. Safaei, S. Sahmani, Buckling and postbuckling response of nonlocal strain gradient porous functionally graded micro/nano-plates via NURBS-based isogeometric analysis, Thin Wall. Struct. 159 (2021) 107231.

[22] F. Fan, C. Xiumei, S. Sahmani, B. Safaei, Isogeometric thermal postbuckling analysis of porous FGM quasi-3D nanoplates having cutouts with different shapes based upon surface stress elasticity, Compos. Struct. 262 (2021) 113604.

[23] F. Fan, S. Sahmani, B. Safaei, Isogeometric nonlinear oscillations of nonlocal strain gradient PFGM micro/nano-plates via NURBS-based formulation, Compos. Struct. 255 (2021) 112969.

[24] S. Zhao, Z. Zhao, Z. Yang, L. Ke, S. Kitipornchai, J. Yang, Functionally graded graphene reinforced composite structures: A review, Eng. Struct. 210 (2020) 110339.

[25] Z. Yang, C. Feng, J. Yang, Y. Wang, J. Lv, A. Liu, J. Fu, Geometrically nonlinear buckling of graphene platelets reinforced dielectric composite (GPLRDC) arches with rotational end restraints, Aerosp. Sci. Technol. 107 (2020) 106326.

[26] Z. Yang, M. Tam, Y. Zhang, S. Kitipornchai, J. Lv, J. Yang, Nonlinear dynamic response of FG graphene platelets reinforced composite beam with edge cracks in thermal environment, Int. J. Struct. Stab. Dy. 20 (2020) 2043005.

[27] H. Wu, J. Yang, S. Kitipornchai, Dynamic instability of functionally graded multilayer graphene nanocomposite beams in thermal environment, Compos. Struct. 162 (2017), 244-254.

[28] M. A. Rafiee, J. Rafiee, Z. Wang, H. Song, Z. Z. Yu, N. Koratkar, Enhanced mechanical properties of nanocomposites at low graphene content, Acs Nano. 3 (2009) 3884-3890.

[29] M. A. Rafiee, J. Rafiee, I. Srivastava, Z. Wang, H. Song, Z. Z. Yu, N. Koratkar, Fracture and fatigue in graphene nanocomposites, Small. 6 (2010) 179-183.

[30] J. Liu, H. Yan, K. Jiang, Mechanical properties of graphene platelet-reinforced alumina ceramic composites, Ceram. Int. 39(2013) 6215-6221.

[31] J. Liu, Z. Li, H. Yan, K. Jiang, Spark plasma sintering of alumina composites with graphene platelets and silicon carbide nanoparticles, Adv. Eng. Mater. 16 (2014), 1111-1118.

[32] L. C. Tang, Y. J. Wan, D. Yan, Y. B. Pei, L. Zhao, Y. B. Li, G. Q. Lai, The effect of graphene dispersion on the mechanical properties of graphene/epoxy composites, Carbon. 60 (2013) 16-27.

[33] S. Kitipornchai, D. Chen, J. Yang, Free vibration and elastic buckling of functionally graded porous beams reinforced by graphene platelets, Mater. Design. 116 (2017) 656-665.

[34] D. Chen, J. Yang, S. Kitipornchai, Nonlinear vibration and postbuckling of functionally graded graphene reinforced porous nanocomposite beams, Compos. Sci. Technol. 142 (2017), 235-245.

[35] M.Tam, Z. Yang, S. Zhao, H. Zhang, Y. Zhang, J. Yang, Nonlinear bending of elastically restrained functionally graded graphene nanoplatelet reinforced beams with an open edge crack, Thin Wall. Struct. 156 (2020) 106972.

[36] K. Li, D. Wu, X. Chen, J. Cheng, Z. Liu, W. Gao, M. Liu, Isogeometric analysis of functionally graded porous plates reinforced by graphene platelets, Compos. Struct. 204 (2018) 114-130.

[37] Y. H. Dong, L. W. He, L. Wang, Y. H. Li, J. Yang, Buckling of spinning functionally graded graphene reinforced porous nanocomposite cylindrical shells: An analytical study, Aerosp. Sci. Technol. 82 (2018) 466-478.

[38] Y. H. Dong, Y. H. Li, D. Chen, J. Yang, Vibration characteristics of functionally graded graphene reinforced porous nanocomposite cylindrical shells with spinning motion, Compos. Part B- Eng. 145 (2018) 1-13.

[39] Y. Q. Wang, C. Ye, J. W. Zu, Nonlinear vibration of metal foam cylindrical shells reinforced with graphene platelets, Aerosp. Sci. Technol. 85 (2019), 359-370.

[40] A. Liu, Z. Yang, H. Lu, J. Fu, Y. L. Pi, Experimental and analytical investigation on the in-plane dynamic instability of arches owing to parametric resonance, J. Vib. Control. 24 (2018) 4419-4432.

[41] A. Liu, H. Lu, J. Fu, Y. L. Pi, Y. Huang, J. Li, Y. Ma, Analytical and experimental studies on out-of-plane dynamic instability of shallow circular arch based on parametric resonance, Nonlinear Dynam. 87 (2017) 677-694.

[42] A. Liu, Z. Yang, M. A. Bradford, Y. L. Pi, Nonlinear dynamic buckling of fixed shallow arches under an arbitrary step radial point load, J. Eng. Mech. 144 (2018) 04018012.

[43] D. Wu, A. Liu, Y. Huang, Y. Huang, Y. Pi, W. Gao, Time dependent uncertain free vibration analysis of composite CFST structure with spatially dependent creep effects, Appl. Math. Model. 75 (2019) 589-606.

[44] Z. Yang, A. Liu, Y. L. Pi, J. Fu, Z. Gao, Nonlinear dynamic buckling of fixed shallow arches under impact loading: An analytical and experimental study, J. Sound. Vib. 487 (2020) 115622.

[45] Y. L. Pi, M. A. Bradford, Dynamic buckling of shallow pin-ended arches under a sudden central concentrated load, J. Sound. Vib. 317 (2008) 898-917.

[46] Y. L. Pi, M. A. Bradford, Nonlinear dynamic buckling of pinned-fixed shallow arches under a sudden central concentrated load, Nonlinear Dynam. 73 (2013) 1289-1306.

[47] Y. L. Pi, M. A. Bradford, W. Qu, Energy approach for dynamic buckling of shallow fixed arches under step loading with infinite duration, Struct. Eng. Mech. 35 (2010) 555-570.

[48] Z. Yang, J. Yang, A. Liu, J. Fu, Nonlinear in-plane instability of functionally graded multilayer graphene reinforced composite shallow arches, Compos. Struct. 204 (2018) 301-312.

[49] Z. Yang, Y. Huang, A. Liu, J. Fu, D. Wu, Nonlinear in-plane buckling of fixed shallow functionally graded graphene reinforced composite arches subjected to mechanical and thermal loading, Appl. Math. Model. 70 (2019) 315-327.

[50] Z. Yang, A. Liu, J. Yang, J. Fu, B. Yang, Dynamic buckling of functionally graded graphene nanoplatelets reinforced composite shallow arches under a step central point load, J. Sound. Vib. 465 (2020), 115019.

[51] Z. Yang, S. Zhao, J. Yang, J. Lv, A. Liu, J. Fu, In-plane and out-of-plane free vibrations of functionally graded composite arches with graphene reinforcements, Mech. Adv. Mater. Struc. (2020) 1-11. (doi.org/10.1080/15376494.2020.1716420)

[52] Z. Yang, J. Xu, H. Lu, J. Lv, A. Liu, J. Fu, Multiple equilibria and buckling of functionally graded graphene nanoplatelet-reinforced composite arches with pinned-fixed end, Crystals, 10 (2020) 1003.

[53] Z. Yang, A. Liu, J. Yang, S-K. Lai, J. Lv, J. Fu, Analytical prediction for nonlinear buckling of elastically supported FG-GPLRC arches under a central point load, Materials, 14 (2021) 2026.

[54] Z. Liu, C. Yang, W. Gao, D. Wu, G. Li, Nonlinear behaviour and stability of functionally graded porous arches with graphene platelets reinforcements, Int. J. of Eng. Sci. 137 (2019), 37-56.

[55] Z. Li, J. Zheng, Y. Chen, Q. Sun, Z. Zhang, Effect of temperature variations on the stability mechanism of the confined functionally graded porous arch with nanocomposites reinforcement under mechanical loading, Compos. Part B-Eng. 176 (2019) 107330.

[56] Z. Li, Y. Chen, J. Zheng, Q. Sun, Thermal-elastic buckling of the arch-shaped structures with FGP aluminum reinforced by composite graphene platelets, Thin Wall. Struct. 157 (2020) 107142.

[57] S. Zhao, Z. Yang, S. Kitipornchai, J. Yang, Dynamic instability of functionally graded porous arches reinforced by graphene platelets, Thin Wall. Struct. 147 (2020) 106491.

[58] A.P. Roberts, E.J. Garboczi, Elastic moduli of model random three-dimensional closed-cell cellular solids, Acta Mater., 49 (2001) 189-197.

[59] Y. L. Pi, M. A. Bradford, Non-linear in-plane postbuckling of arches with rotational end restraints under uniform radial loading, Int. J. Nonlin. Mech. 44 (2009) 975-989.